MEASUREMENT OF AURORAL ELECTRIC FIELDS WITH AN ANTARCTIC SOUNDING ROCKET S-310JA-7
1. DC ELECTRIC FIELD

Toshio OGAWA, Masahiko MAKINO, Sachiko HAYASHIDA,
Geophysical Institute, Kyoto University, Kitashirakawa Oiwake-cho, Sakyo-ku, Kyoto 606

Hisao YAMAGISHI, Ryoichi FUJII, Hiroshi FUKUNISHI, Takeo HIRASAWA
National Institute of Polar Research, 9-10, Kaga 1-chome, Itabashi-ku, Tokyo 173

and

Masanori NISHINO
Research Institute of Atmospherics, Nagoya University, 13, Honohara 3-chome, Toyokawa 442

Abstract: The results are given on the DC electric field in an active auroral arc and outside the equatorside of it observed with two pairs of orthogonal double probes launched by an Antarctic sounding rocket S-310JA-7 at 191550 UT on March 27, 1978 at Syowa Station. The north-south component of the observed electric field was northward (equatorward) in the arc, and southward (poleward) outside the equatorside of the arc with a magnitude of about 20 mV/m. The east-west component was mostly westward throughout the rocket flight and smaller (about 5 mV/m) in the arc and larger (about 50 mV/m) outside the arc. Anti-correlation of the electric field and precipitating particles is evident. An examination of the oppositely inward directed electric fields in the meridional cross section suggests an electrostatic potential configuration responsible for the acceleration of precipitating particles. The observed westward component would have been originated in the large scale earthward plasma convection in the magnetosphere.

1. Introduction

In recent years a number of auroral electric field measurements have been made by means of several different techniques using rockets (*e.g.* BERING *et al.*, 1975; EDWARDS *et al.*, 1976; MAYNARD *et al.*, 1977; EVANS *et al.*, 1977; CARLSON and KELLEY, 1977; PETELSKI *et al.*, 1978; OGAWA *et al.*, 1979; CAHILL *et al.*, 1980), satellites (*e.g.* MOZER *et al.*, 1977; AGGSON and HEPPNER, 1977; TORBERT and MOZER, 1978; MOZER *et al.*, 1979), balloons (*e.g.* HOLZWORTH *et al.*, 1977), barium clouds (*e.g.* SHAWHAN *et al.*, 1978) and incoherent scatter radars (*e.g.* DE LA BEAUJARDIERE *et al.*, 1977; HORWITZ *et al.*, 1978a, b; NIELSEN and GREENWALD, 1978; BAUMJOHANN

et al., 1980). The auroral phenomena are so various and complex that the available electric field data obtained previously are not always consistent with each other (see *e.g.* STERN, 1977; KAMIDE, 1979) and we need more experimental data corresponding to various phases of auroral activity together with those of other related parameters.

An experiment with an Antarctic sounding rocket S-310JA-7 was planned as one of the IMS projects to measure DC and AC electric fields for investigating correlations of electrostatic plasma waves generated in the precipitating auroral particles. The result of DC electric field measurement is given in this report.

2. Instrumentation

The electric field detector consists of two pairs of double probes. The pairs are separate 47 cm along the rocket axis. Four spherical probes are attached at the ends of paired booms. The distance of paired probes is 2.45 m.

The spherical probes are of 4 cm in diameter, gold-plated and aquadag-coated. Inside the spherical probes are contained high impedance preamplifiers. The input resistance of the preamplifiers is 1×10^9 ohms.

Potential difference from the preamplifier outputs is amplified separately by 20.2 db for DC component and by 43.3 db for AC component respectively. The corner frequency of the high pass filter for AC signals is 5 Hz. The upper limits of the frequency response of the used telemeter are 25 Hz (IRIG Channel No. 6) for the upper probes and 59 Hz (No. 9) for the lower probes for the DC components and 220 Hz (No. 13) for the AC component.

3. Observation

The Antarctic sounding rocket S-310JA-7 was launched at 191550 UT (221550 EST) on March 27, 1978 from Syowa Station (geographic lat. 69.00°S and long.

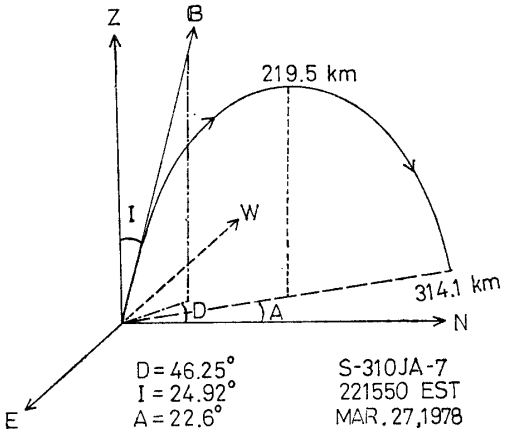

Fig. 1. Trajectory of the Antarctic sounding rocket S-310JA-7 which was launched on March 27, 1978 from Syowa Station.

39.58°E; geomagnetic lat. 69.81°S and long. 78.51°E; L value=6.1) into an active auroral arc. Our experiment on this rocket measured the DC and AC (5–220 Hz) electric fields. Besides the electric fields the onboard instruments also have made the *in situ* measurements of plasma waves in the frequency range of 10 Hz–8 MHz, auroral energetic particles in the energy range of 0.1–10 keV, auroral X-rays (>4 keV), electron density, and electron temperature.

The rocket was launched at the elevation angle of 75° and the azimuth of 326°. The rocket reached the maximum height of 219.5 km at the azimuth of 339° within 230 s after the launch. The total horizontal distance of the rocket flight was 314.1 km. The rocket flight trajectory is schematically shown in Fig. 1.

4. Data Analysis

Total DC electric fields ($|\boldsymbol{E}+\boldsymbol{V}\times\boldsymbol{B}|$) observed with the two pairs of double probes are shown with flight times and altitudes in Figs. 2 and 3 respectively, where $\boldsymbol{E}$ is the static electric field to be measured, $\boldsymbol{V}$ is the rocket velocity and $\boldsymbol{B}$ is the geomagnetic flux density. The estimated induced electric field ($|\boldsymbol{V}\times\boldsymbol{B}|$) is also plotted in the figures. All four booms deployed successfully and the electric field estimated from the data collected by the upper boom pair was consistent with that obtained by the lower boom pair. Such a comparison is made in Figs. 2 and 3. The satisfactory agreement between the two measurements during both rocket ascent and descent argues strongly for the conclusion that the measured electric fields are natural fields. Because all booms deployed properly during the flight, the electric field parallel to the rocket axis is to be determined by combining the measurements of the electric potential at the middle point between two probes on the upper booms with that on the lower booms. Such measurement has been done but the potential difference obtained

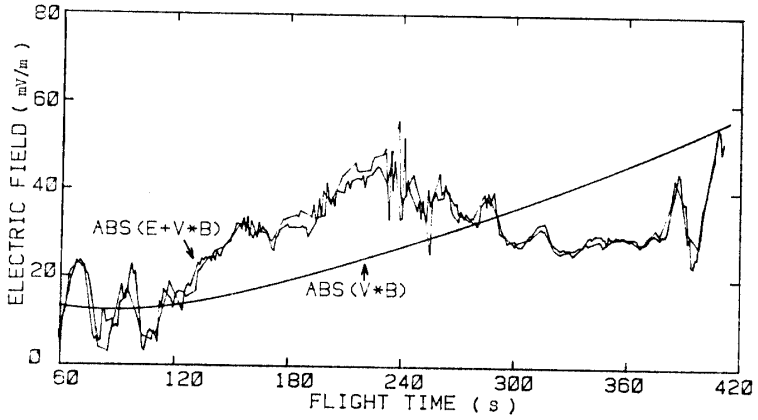

Fig. 2. Observed electric fields ($|\boldsymbol{E}+\boldsymbol{V}\times\boldsymbol{B}|$) and calculated induced electric field ($|\boldsymbol{V}\times\boldsymbol{B}|$) plotted as a function of flight time.

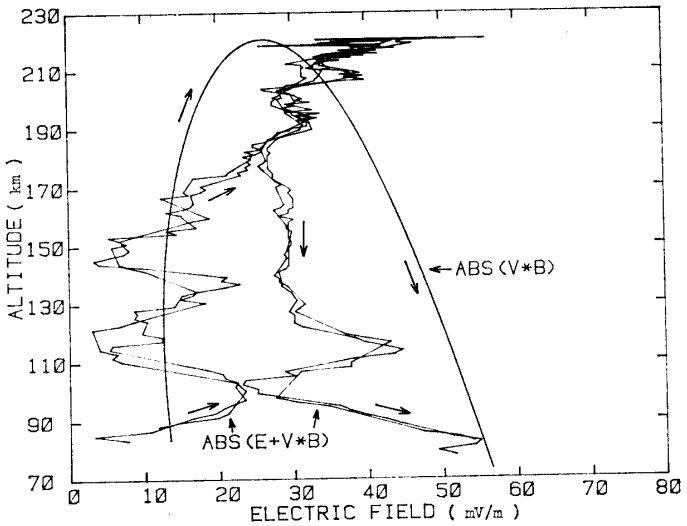

Fig. 3. Altitude profile of the observed electric fields ($|\boldsymbol{E}+\boldsymbol{V}\times\boldsymbol{B}|$) and the calculated induced electric field ($|\boldsymbol{V}\times\boldsymbol{B}|$).

was so large, of the order of 500 mV/m, that we do not use it in this data analysis at the moment.

Precession of the rocket axis was estimated from the on-board geomagnetic aspect-sensor (GAZ). The minimum angle between the precession axis and the geomagnetic field line was 1° at the flight times of 120 s and 312 s; the precession period was 192 s. The maximum angle was 11.6°. Using the rocket aspect information the Earth-referenced electric field can be estimated from the probe-observed electric fields. Details of the data analysis technique are given in the Appendix.

5. Results

The Earth-referenced electric fields were estimated by using the assumed electric field parallel to the geomagnetic field line. The calculated results are shown in Figs. 4a, b and 5a, b with both rocket flight times and altitudes by using the assumed parallel electric fields of 0 and 10 mV/m respectively, where the magnetic coordinate system is employed.

With the data from the radar transponder the rocket altitude as a function of time, $H(t)$, was approximated in the form:

$$H(t)=-24.99+2.108t-0.004519t^2. \tag{1}$$

The calculated altitudes by eq. (1) have been plotted in Figs. 4 and 5. The maximum altitude attained to 220.8 km which is 1.3 km larger than the value of 219.5 km obtained experimentally in Fig. 1. This difference, however, does not have any serious effect on the discussion to be made.

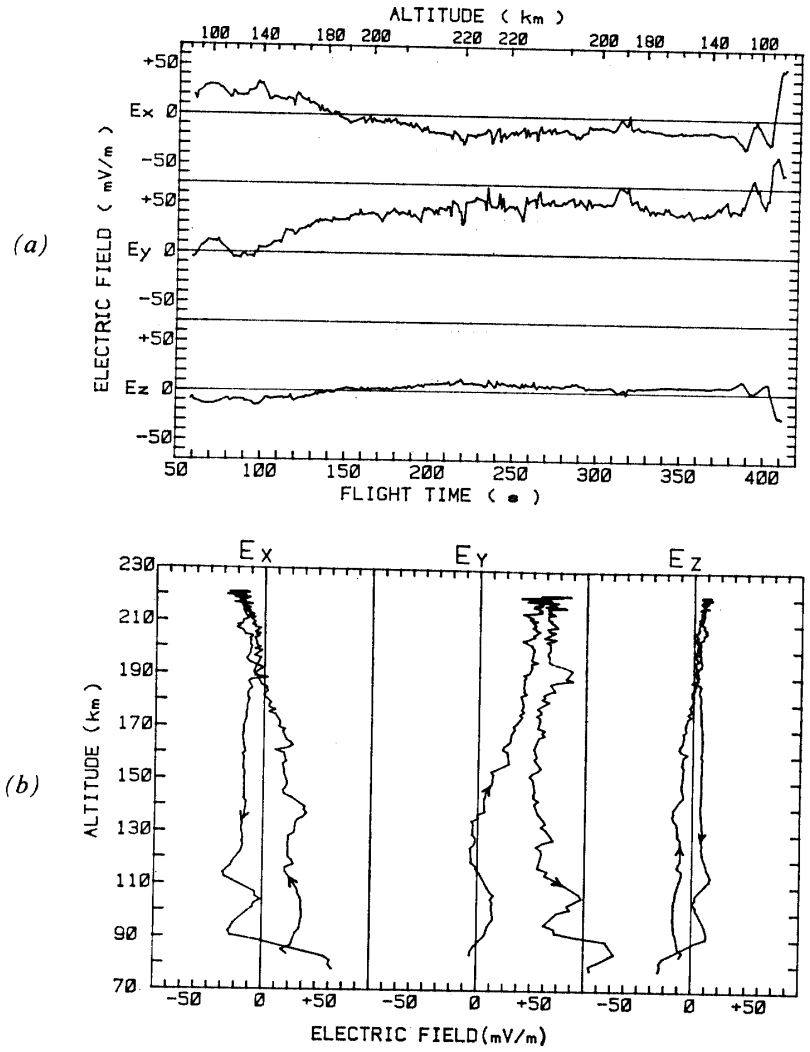

Fig. 4. North, west and vertical (upward) components of the electric field E_x, E_y, E_z, respectively, vs. rocket flight time and altitude (a) and vs. altitude (b) assuming no parallel electric field.

The magnetic-northward component (E_x) increased by about 5 mV/m with the assumed parallel electric-field value of 10 mV/m as shown in Figs. 4 and 5. The northward component was initially 20~30 mV/m. It decreased with height, attained to zero at the height of about 190 km, then came to about −20 mV/m at the maximum height. During the rocket descent it again came to zero at about 190 km and then decreased to about −10~−20 mV/m. It had a large variation in the altitude range of 90–110 km.

The magnetic-westward component (E_y) did not change in the two cases shown in Figs. 4 and 5. It was about 10 mV/m at the auroral height, about −5 mV/m above the auroral height, then increased with height up to about 50 mV/m at the maximum

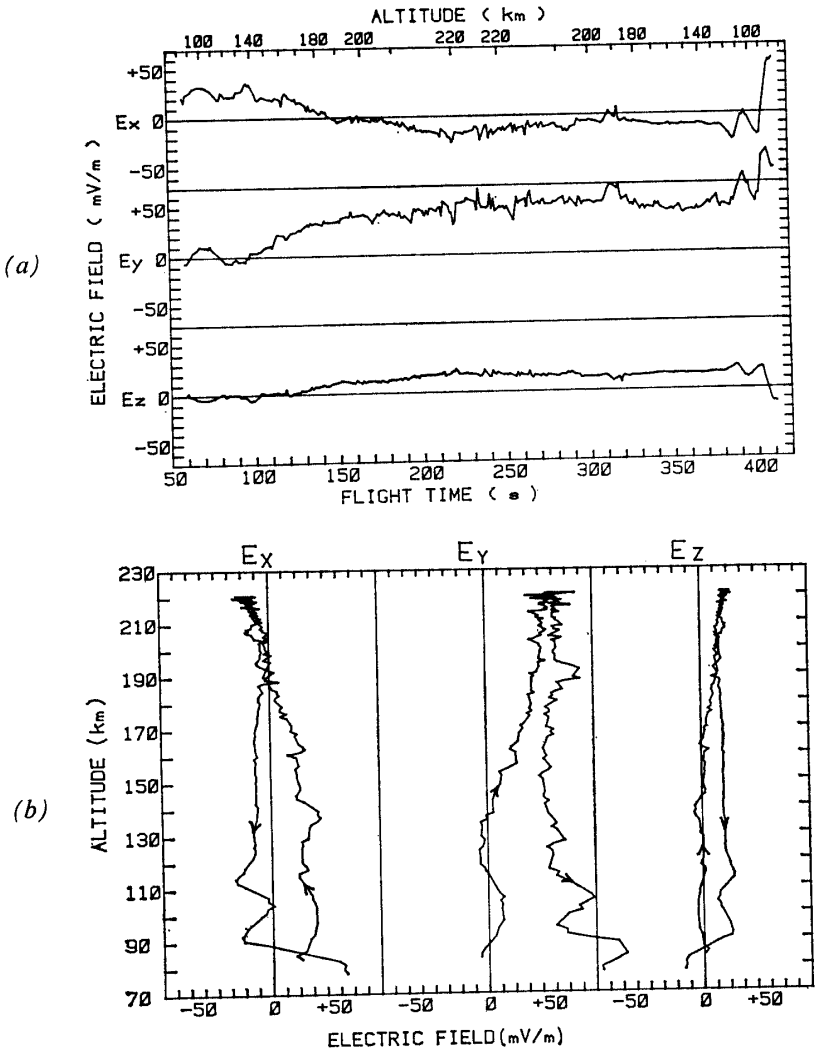

Fig. 5. North, west and vertical (upward) components of the electric field E_x, E_y, E_z, respectively, vs. rocket flight time and altitude (a) and vs. altitude (b) assuming 10 mV/m parallel electric field.

height of 220.8 km. During the rocket descent the westward field decreased to 40 mV/m at the altitude of 150 km and then increased up to about 100 mV/m at the height of about 90 km. It had the large variation in the range of 90–110 km as did the northward component as well.

It was a natural result that the vertical electric-field component (E_z) had the most significant effect by the assumed parallel electric field. During the rocket ascent the vertical electric-field component was initially about -10 and 0 mV/m and increased to 10 and 20 mV/m depending on the assumed parallel electric field of 0 and 10 mV/m respectively, while in the descent period it stayed at about the same magni-

tudes. It had the variation of about 10 mV/m in the altitude range of 90–110 km as in the other two component fields.

6. Discussion

An intense auroral substorm started equatorward of Syowa Station just before the rocket launching time. The records of geomagnetic H component, and the cosmic noise absorption (CNA) at 30 MHz during the rocket flight time are shown in Fig. 6 in which the rocket launching time is indicated by a dashed line.

The time and space distribution of aurora observed with the 5577 Å-photometer is shown in Fig. 7. The rocket trajectory was projected along the geomagnetic field lines on to the auroral height (100 km). It is realized in Fig. 7 that the rocket was launched into the most active region at the auroral break-up time, and traversed the edge of the equatorward-traveling arc near the end of the flight.

All-sky camera photographs during the rocket flight time are shown in Fig. 8. The positions of the rocket projected on the 100 km level along the geomagnetic field lines are indicated by spots and the reduced horizontal electric fields with the assumed

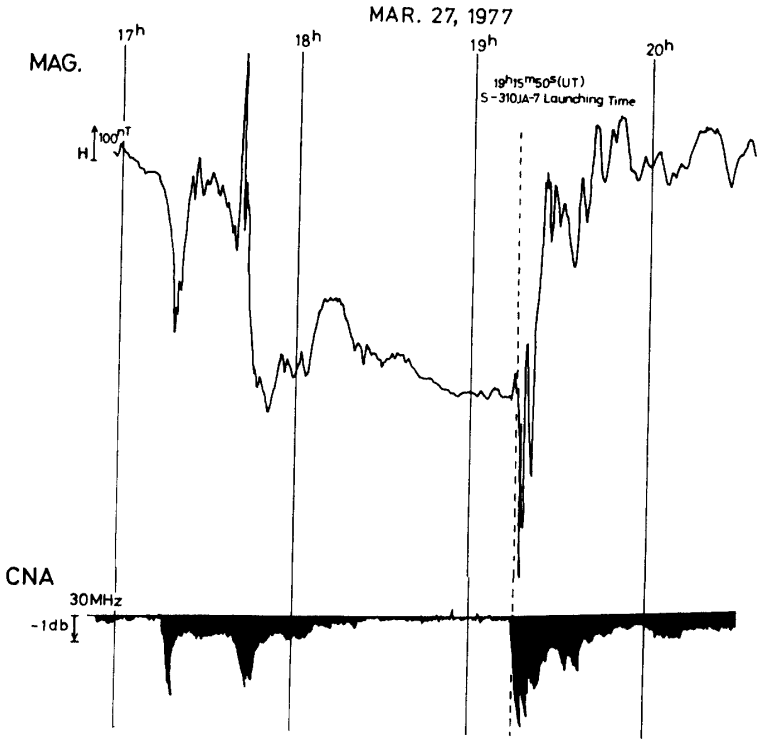

Fig. 6. Geomagnetic field variation (horizontal component) and cosmic noise absorption (CNA) observed at Syowa Station.

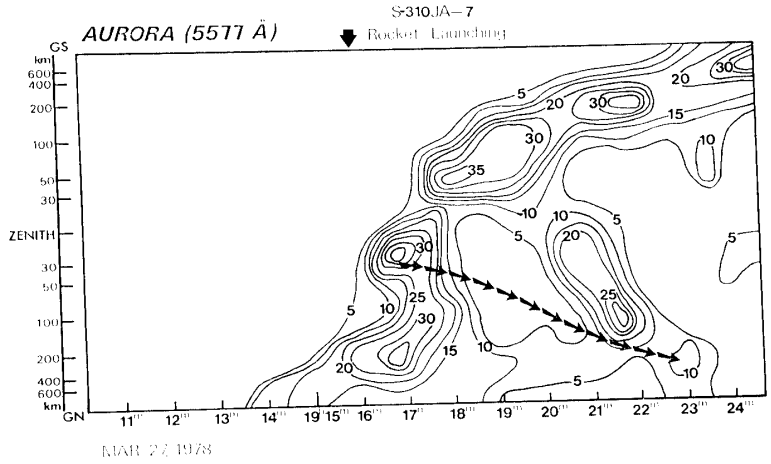

Fig. 7. The time and space distribution of aurora. The rocket trajectory was projected along the geomagnetic field lines on to the auroral height (100 km).

zero parallel electric field are scaled by bars. The all-sky pictures shown in Fig. 8 indicate a typical auroral arc motion during the substorm time. It is seen in the pictures during the rocket ascent that a bright arc moved rapidly southward (poleward). Then this arc was separated into two arcs at 260 s. The poleward arc moved further poleward while the other one moved equatorward forming a spiral structure at about 300 s. The equator edge of this spiral became a new arc at 320 s, and the curls traveling westward were seen at 340–370 s.

When the rocket encountered the poleward expanding arc, the northward (equatorward) electric field is dominant inside and adjacent to the equatorside of the arc. In the region outside the equatorside of the arc the predominant electric field was westward with a magnitude of about 50 mV/m. It is found from a comparison of the pictures at 60 s and 120 s or later that the electric field is smaller in the arc and larger outside the aurora. Anticorrelation of the electric field and precipitating particles is evident.

There appeared an electric field hump with a magnitude about 20 mV/m at the rocket flight time of 310 s when the probes measured the electric field at the edge of the breaked-up equatorward-traveling curl-type arc. The poleward electric field diminished in magnitude to about 10 mV/m during this period (about 10 s). The edge of this curl-type arc kept traveling equatorward. The direction of this movement agrees with the direction of $\boldsymbol{E} \times \boldsymbol{B}$ drift of plasma.

In order to examine more clearly the electric field at various points along the rocket trajectory, the northward and westward vector components were plotted every 15 seconds of the rocket flight time and are given in Figs. 9a and 9b, respectively, where the calculated electric field with the assumed zero parallel electric field was used.

It is difficult to differentiate the spatial profile from the temporal one, but it can

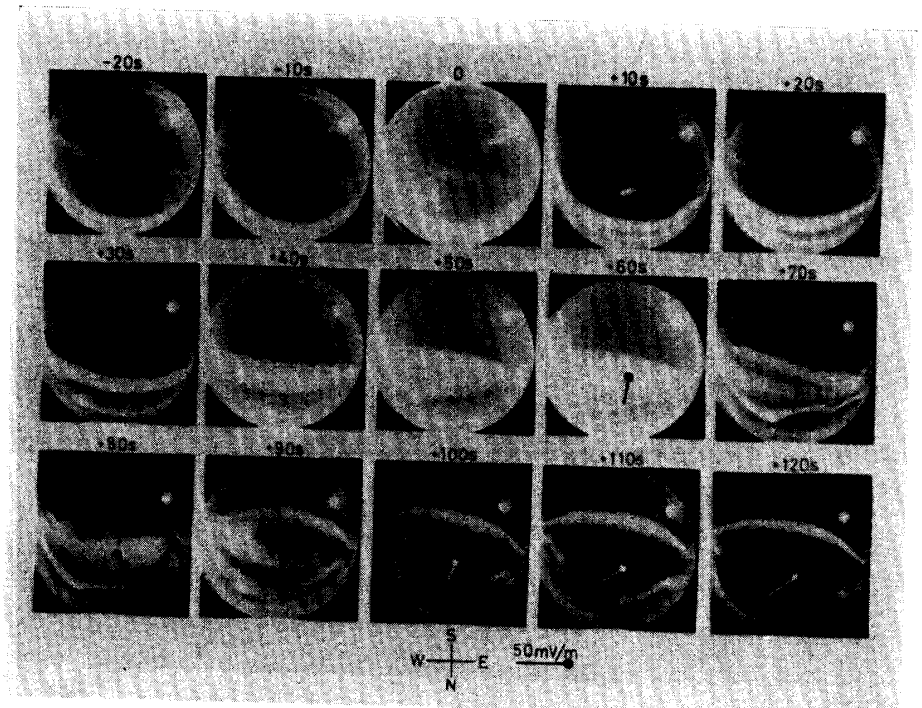

Fig. 8a. From 20 s before the rocket launching to 120 s after the launching.

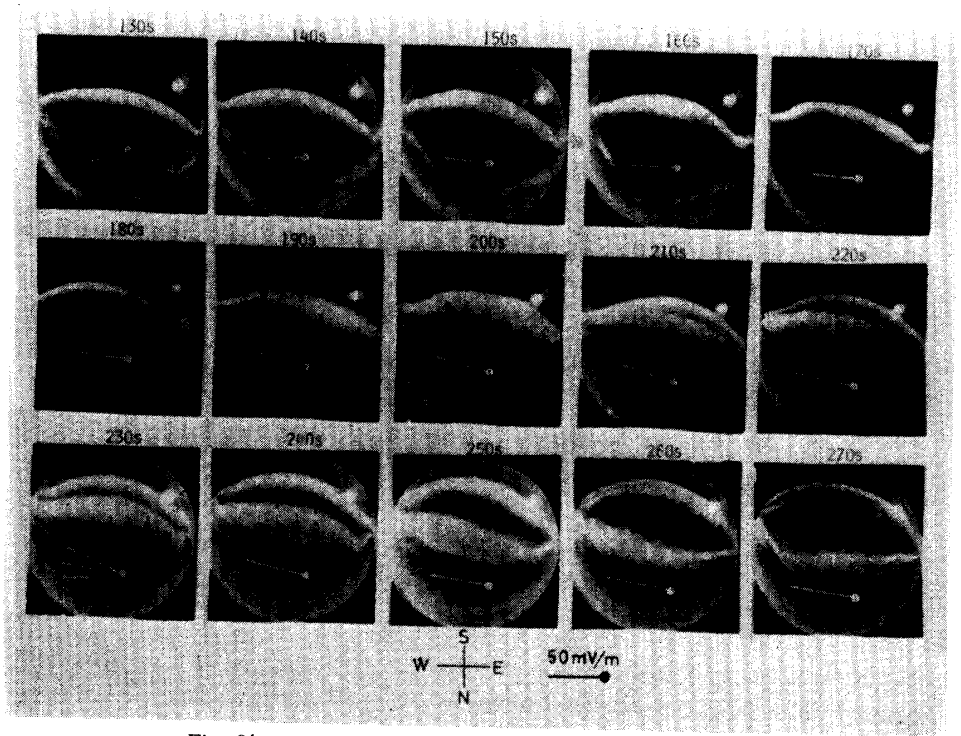

Fig. 8b. From 130 to 270 s of the rocket flight time.

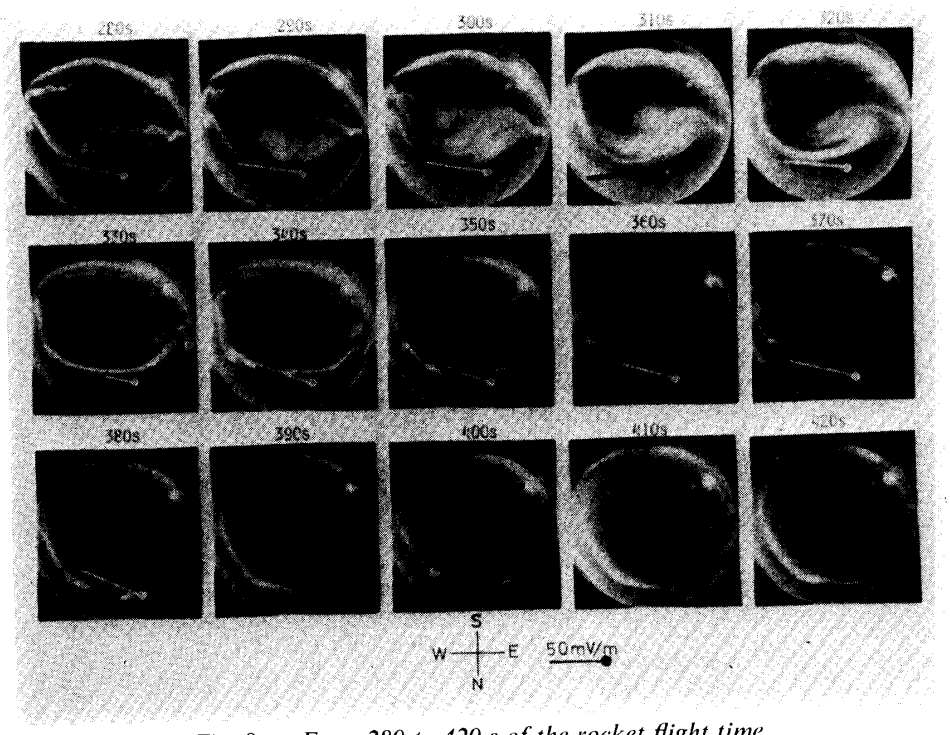

Fig. 8c. From 280 to 420 s of the rocket flight time.

Fig. 8. A series of photographs taken by the all-sky camera. The horizontal electric fields are indicated, projected on the auroral height along the geomagnetic field lines from the rocket positions every 10 s.

be seen in Figs. 9a and 9b that the northward component clearly changed its sign from northward to southward during the rocket flight at an altitude of about 180 km in the equatorside of the auroral arc, while the westward component almost kept its sign throughout the rocket flight although there were some disturbances in and near the auroral arc. The oppositely inward directed electric-field spatial pattern in the magnetic meridional cross-section shown in Fig. 9a suggests a double-structured electrostatic potential configuration which would be responsible for the acceleration of precipitating particles.

MOZER *et al.* (1977) made *in situ* measurements of electric fields by the S3-3 satellite at auroral latitudes and altitudes where particle acceleration process is thought to occur, and found the spatially confined regions of extremely large electric fields whose structure suggests the paired electrostatic shocks that may be associated with particle acceleration.

MOZER (1976) presented the summary of experimental evidence for the existence of electric fields having components parallel to the magnetic field direction in the auroral zone ionosphere below 400 km, and concluded that about 10 mV/m parallel electric fields are frequently observed. The present Antarctic sounding rocket ex-

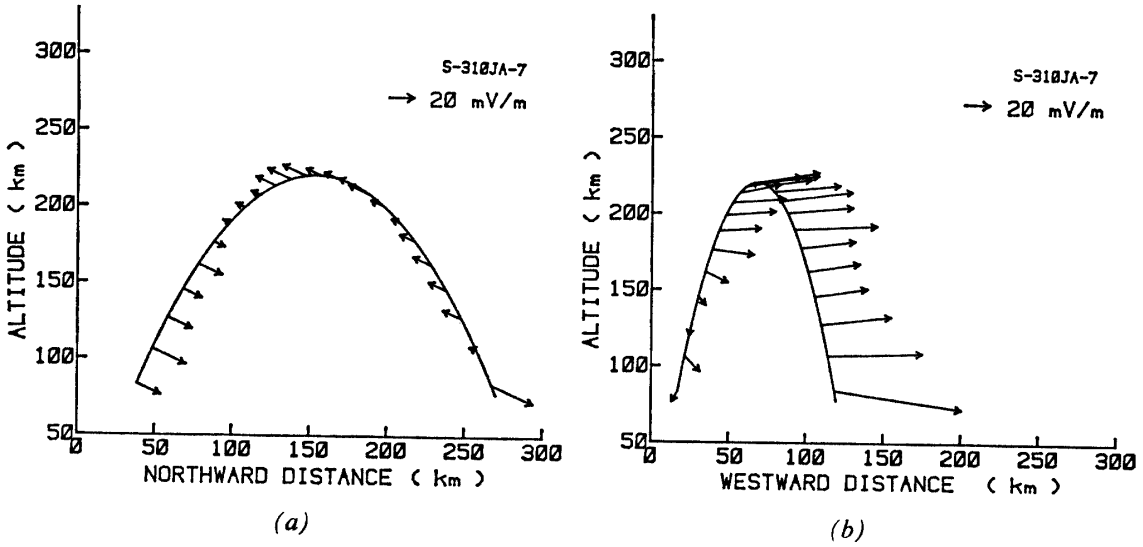

Fig. 9. Electric field projected on the vertical plane superimposed upon the rocket trajectory. (a) Magnetic north and vertical plane. (b) Magnetic west and vertical plane.

periment also observed the very large electric field parallel to the magnetic field, of the order of 500 mV/m, but we need a little more time to conclude the existence of such electric field. Instead of using the experimental data, we assumed the parallel electric fields in the estimation of earth-referenced electric fields from the observed data.

The east-west component of the observed electric field is mostly westward and only reduced in strength inside and adjacent to the auroral arc. This component might be originated in the large-scale earthward plasma convection in the magnetosphere.

We saw in Figs. 4 and 5 that the electric fields in the altitude range of 90–110 km after the rocket flight time of 392 s made large variations. It was found, however, that data quality in this period is poor; the spinmodulated electric field waveforms are distorted. Therefore, we did not pay much attention to this period of data.

Acknowledgments

We wish to express our thanks to the members of the 19th wintering party of the Japanese Antarctic Research Expedition for their effort in launching the rocket and in making the ground-based observations. We are also grateful to Drs. M. KODAMA, F. TOHYAMA and I. AOYAMA for their help in evaluating the rocket attitude.

References

AGGSON, T. L. and HEPPNER, J. P. (1977): Observations of large transient magnetospheric electric fields. J. Geophys. Res., **82**, 5155–5164.

BAUMJOHANN, W., UNTIEDT, T. and GREENWALD, R. A. (1980): Joint two-dimensional observations of ground magnetic and ionospheric electric fields associated with auroral zone currents 1. Three-dimensional current flows associated with a substorm-intensified eastward electrojet. J. Geophys. Res., **85**, 1963–1978.

BERING, M., KELLEY, M. C. and MOZER, F. S. (1975): Observations of an intense field-aligned thermal ion flow and associated intense narrow band electric field oscillations. J. Geophys. Res., **80**, 4612–4620.

CAHILL, L. J., JR., ARNOLDY, R. L. and TAYLOR, W. W. L. (1980): Rocket observations at the northern edge of the eastward electrojet. J. Geophys. Res., **85**, 3407–3413.

CARLSON, C. W. and KELLEY, M. C. (1977): Observation and interpretation of particle and electric field measurements inside and adjacent to an active auroral arc. J. Geophys. Res., **82**, 2349–2360.

DE LA BEAUJARDIERE, O., VONDRAK, R. and BARON, M. (1977): Radar observations of electric fields and currents associated with auroral arcs. J. Geophys. Res., **82**, 5051–5062.

EDWARDS, T., BRYANT, D. A., SMITH, M. J., FAHLESON, U., FÄLTHAMMAR, C. -G. and PEDERSEN, A. (1976): Electric fields and energetic particle precipitation in an auroral arc. Magnetospheric Particles and Fields, ed. by B. M. MCCORMAC. Dordrecht, D. Reidel, 285–289.

EVANS, D. S., MAYNARD, N. C., TRØIM, J., JACOBSEN, T. and EGELAND, A. (1977): Auroral vector electric field and particle comparisons 2. Electrodynamics of an arc. J. Geophys. Res., **82**, 2235–2249.

HOLZWORTH, R. H., BERTHELIER, J. -J., CULLERS, D. K., FAHLESON, U. V., FÄLTHAMMAR, C. -G., HUDSON, M. K., JALONAN, L., KELLEY, M. C., KELLOGG, P. J., TANSKANEN, P., TEMERIN, M. and MOZER, F. S. (1977): The large-scale ionospheric electric field: Its variation with magnetic activity and relation to terrestrial kilometric radiation. J. Geophys. Res., **82**, 2735–2742.

HORWITZ, J. L., DOUPNIK, J. R. and BANKS, P. M. (1978a): Chatanika radar observations of the latitudinal distributions of auroral zone electric fields, conductivities, and currents. J. Geophys. Res., **83**, 1063–1481.

HORWITZ, J. L., DOUPNIK, J. R., BANKS, P. M., KAMIDE, Y. and AKASOFU, S. -I. (1978b): The latitudinal distributions of auroral zone electric fields and ground magnetic perturbations and their response to variations in the interplanetary magnetic field. J. Geophys. Res., **83**, 2071–2084.

KAMIDE, Y. (1979): Recent progress in observational studies of electric fields and currents in the polar ionosphere: A review. Nankyoku Shiryô (Antarct. Rec.), **63**, 61–231.

MAYNARD, N. C., EVANS, D. S., MAEHLUM, B. and EGELAND, A. (1977): Auroral vector electric field and particle comparisons 1. Premidnight convection topology. J. Geophys. Res., **82**, 2227–2234.

MOZER, F. S. (1976): Observations of large parallel electric fields in the auroral ionosphere. Ann. Geophys., **32**, 97–107.

MOZER, F. S., CARLSON, C. W., HUDSON, M. K., TORBERT, R. B., PARADY, B. and YATTEAU, J. (1977): Observation of paired electrostatic shocks in the polar magnetosphere. Phys. Rev. Lett., **38**, 292–295.

MOZER, F. S., CATTELL, C. A., TEMERIN, M., TORBERT, R. B., VON GLINSKI, S., WOLDORFF, M. and

WYGANT, J. (1979): The dc and ac electric field, plasma density, plasma temperature, and field-aligned current experiments on the S3-3 satellite. J. Geophys. Res., **84**, 5875–5884.

NIELSEN, E. and GREENWALD, R. A. (1978): Variations in ionospheric currents and electric fields in association with absorption spikes during the substorm expansion phase. J. Geophys. Res., **83**, 5645–5654.

OGAWA, T., MORITA, M., FUKUNISHI, H., MATSUO, T. and YOSHINO, T. (1979): Nankyoku roketto S-210JA-24, 25-gôki ni yoru denrisô denba no kansoku (Measurements of ionospheric electric fields with Antarctic sounding rockets S-210JA-24 and 25). Nankyoku Shiryô (Antarct. Rec.), **63**, 252–275.

PETELSKI, E. F., FAHLESON, U. and SHAWHAN, S. D. (1978): Models for quasiperiodic electric fields and associated electron precipitation in the auroral zone. J. Geophys. Res., **83**, 2489–2498.

SHAWHAN, S. D., FÄLTHAMMAR, C. -G. and BLOCK, L. P. (1978): On the nature of large auroral zone electric fields at 1-R_E altitude. J. Geophys. Res., **83**, 1049–1054.

STERN, D. P. (1977): Large-scale electric fields in the earth's magnetosphere. Rev. Geophys. Space Phys., **15**, 156–194.

TORBERT, R. B. and MOZER, F. S. (1978): Electrostatic shocks as the source of discrete auroral arcs. Geophys. Res. Lett., **5**, 135–138.

(Received September 1, 1980; Revised manuscript received December 1, 1980)

Appendix. Data Analysis Technique

The rocket rotates with a combination of two quasi-sinusoidal motions with the spin and precession periods. As the probe antenna is perpendicular to the rocket axis, the direction of the antenna varies with time. The electric field in the rocket-fixed coordinate system, $\boldsymbol{E}$, is given by

$$\boldsymbol{E}=\boldsymbol{E}_g+\boldsymbol{V}\times\boldsymbol{B}, \tag{A1}$$

where $\boldsymbol{E}_g$ is the electric field in the Earth-fixed coordinate system, $\boldsymbol{V}$ is the rocket velocity relative to the Earth, and $\boldsymbol{B}$ is the Earth's magnetic field. We observe the electric field, $\boldsymbol{E}_R$, which is projected on the spin plane of the rocket. $\boldsymbol{E}_R$ is given by

$$\boldsymbol{E}_R=\boldsymbol{E}-(\boldsymbol{e}_s\cdot\boldsymbol{E})\boldsymbol{e}_s, \tag{A2}$$

where $\boldsymbol{e}_s$ is the spin-axis unit vector (see Fig. A1). We, therefore, analyze data according to the following procedure:

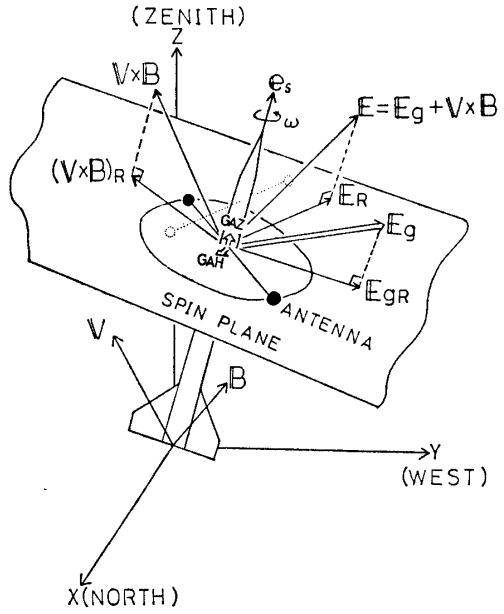

Fig. A1. Schematic coordinates of vectors used for analysis of the rocket electric-field experiment.

1) the determination of the precession axis vector,
2) the determination of the spin axis vector,
3) the calculation of three components of the observed electric field $\boldsymbol{E}_R$,
4) the removal of the induced electric field $\boldsymbol{V}\times\boldsymbol{B}$, and
5) the calculation of the Earth-fixed electric field with the assumption of the electric field parallel to the geomagnetic field line.

A1. The determination of the precession axis vector

We use the geographic coordinate system (x, y, z), where x, y and z are northward, westward, and upward axes, respectively. The unit axis vectors are $\boldsymbol{e}_x$, $\boldsymbol{e}_y$, and $\boldsymbol{e}_z$. The angle between the rocket axis and the geomagnetic field line is ξ. An angle, η, between the precession axis and the geomagnetic field line is given by

$$\eta_1=(\xi_{max}+\xi_{min})/2, \tag{A1-1}$$

$$\eta_2=(\xi_{max}-\xi_{min})/2, \tag{A1-2}$$

where ξ_{max} is the maximum value of ξ and ξ_{min} is the minimum value of ξ (see Fig. A2). The zenith angle of the precession axis is χ. The geomagnetic-field unit vector

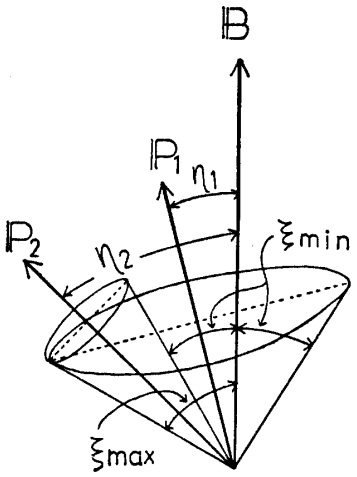

*Fig. A2. Relation between the rocket precession axis (**P**) and a geomagnetic field line (**B**).*

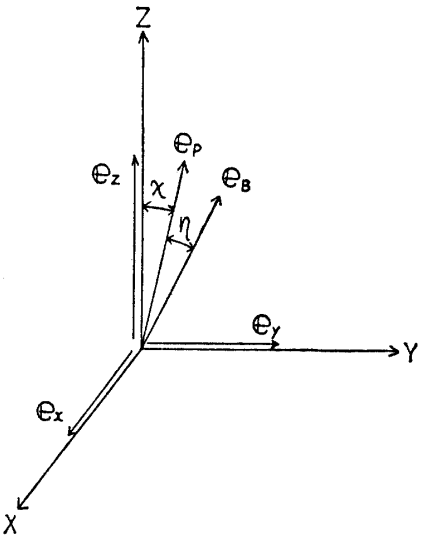

Fig. A3. Definitions of the zenith angle (χ) of the precession axis ($\boldsymbol{e}_p$) and the angle between $\boldsymbol{e}_p$ and geomagnetic field ($\boldsymbol{e}_B$).

is $\boldsymbol{e}_B(e_{Bx}, e_{By}, e_{Bz})$. We assume that the precession axis vector is $\boldsymbol{e}_p(e_{px}, e_{py}, e_{pz})$ (see Fig. A3). The inner product of $\boldsymbol{e}_p$ and $\boldsymbol{e}_B$ is expressed as

$$\boldsymbol{e}_p\cdot\boldsymbol{e}_B=\cos\eta, \tag{A1-3}$$

that is,

$$e_{px}e_{Bx}+e_{py}e_{By}+e_{pz}e_{Bz}=\cos\eta. \tag{A1-4}$$

The inner product of $\boldsymbol{e}_p$ and $\boldsymbol{e}_z$ is expressed as

$$\boldsymbol{e}_p\cdot\boldsymbol{e}_z=\cos\chi, \tag{A1-5}$$

that is,

$$e_{pz}=\cos\chi. \tag{A1-6}$$

As $\boldsymbol{e}_p$ is the unit vector,

$$e_{px}^2+e_{py}^2+e_{pz}^2=1. \tag{A1-7}$$

We obtain e_{px}, e_{py} and e_{pz} from eqs. (A1-4), (A1-6) and (A1-7). We substitute η_1 and η_2 in eq. (A1-4) and calculate the spin axis vectors for the two cases, respectively. Equations (A1-4), (A1-6), and (A1-7) combine to yield

$$e_{px}e_{Bx}+e_{py}e_{By}+\cos\chi\ e_{Bz}=\cos\eta, \tag{A1-8}$$

and

$$e_{px}^2+e_{py}^2=\sin^2\chi. \tag{A1-9}$$

We can rewrite eq. (A1-8) in the form

$$e_{px}=(\cos\eta-\cos\chi\ e_{Bz}-e_{py}e_{By})/e_{Bx}. \tag{A1-10}$$

By substituting e_{px} in eq. (A1-9), we obtain an equation as

$$\left(1+\frac{e_{By}^2}{e_{Bx}^2}\right)e_{py}^2-2\ \{(\cos\eta-\cos\chi\ e_{Bz})e_{By}/e_{Bx}^2\}\ e_{py}$$
$$+(\cos\eta-\cos\chi\ e_{Bz})^2/e_{Bx}^2-\sin^2\chi=0. \tag{A1-11}$$

The solution to eq. (A1-11) can be expressed as

$$e_{py}=\frac{-b\pm\sqrt{b^2-ac}}{a}, \tag{A1-12}$$

where

$$a=\left(1+\frac{e_{By}^2}{e_{Bx}^2}\right) \tag{A1-13}$$

$$b=-(\cos\eta-\cos\chi\ e_{Bz})e_{By}/e_{Bx}^2 \tag{A1-14}$$

$$c=(\cos\eta-\cos\chi\ e_{Bz})^2/e_{Bx}^2-\sin^2\chi. \tag{A1-15}$$

By substituting e_{py} in eq. (A1-10), we obtain e_{px}. If $b^2-ac<0$, we reject the angle η because such a geometric relation between the angle η and χ does not exist. If $b^2-ac>0$, we calculate two e_{py}'s, respectively, because there are two roots in eq. (A1-12). In order to determine the precession axis vector, we need data of the time-varying zenith angle of the spin axis. Let D be the horizontal angle of $\boldsymbol{e}_p$ from the geographic north, then D is given by

$$\left.\begin{aligned} D&=\text{Arctan}\left(\frac{e_{py}}{e_{px}}\right)+\pi, && (\text{if } e_{px}<0)\\ D&=\text{Arctan}\left(\frac{e_{py}}{e_{px}}\right), && (\text{if } e_{px}>0)\\ D&=0. && (\text{if } e_{px}=0) \end{aligned}\right\} \qquad \text{(A1-16)}$$

A2. The determination of the rocket spin-axis vector

The zenith angle and the horizontal angle of the rocket precession axis are χ and D, respectively. We use the rocket precession coordinate system (x', y', z'); z'-axis is the precession axis and x'-axis is perpendicular to y-axis of the geographic coordinate system (x, y, z). We consider a coordinate transformation from (x, y, z) to (x', y', z') (see Fig. A4).

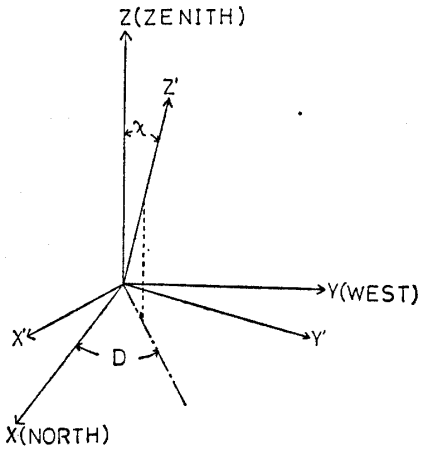

Fig. A4. Transformation of the geographic coordinate system (x, y, z) to the precession coordinate system (x', y', z').

$$\begin{pmatrix} x' \\ y' \\ z' \end{pmatrix} = \begin{pmatrix} l_1 & m_1 & n_1 \\ l_2 & m_2 & n_2 \\ l_3 & m_3 & n_3 \end{pmatrix} \begin{pmatrix} x \\ y \\ z \end{pmatrix}. \qquad \text{(A2-1)}$$

These l_i, m_i, n_i $(i=1,2,3)$ satisfy the following conditions;

$$l_i^2+m_i^2+n_i^2=1, \qquad i=1, 2, 3 \qquad \text{(A2-2)}$$

$$l_i l_j+m_i m_j+n_i n_j=0, \qquad i\neq j \qquad \text{(A2-3)}$$

$$\sum_{i=1}^{3} l_i^2=\sum_{i=1}^{3} m_i^2=\sum_{i=1}^{3} n_i^2=1, \qquad \text{(A2-4)}$$

$$\sum_{i=1}^{3} l_i m_i=\sum_{i=1}^{3} m_i n_i=\sum_{i=1}^{3} n_i l_i=0. \qquad \text{(A2-5)}$$

Let axis unit vectors of (x, y, z) be $(\boldsymbol{i}, \boldsymbol{j}, \boldsymbol{k})$ respectively, and let axis unit vectors of (x', y', z') be $(\boldsymbol{i}', \boldsymbol{j}', \boldsymbol{k}')$ respectively. Then, we obtain the following relations:

$$\boldsymbol{i}' \cdot \boldsymbol{i} = l_1,\ \boldsymbol{i}' \cdot \boldsymbol{j} = m_1,\ \boldsymbol{i}' \cdot \boldsymbol{k} = n_1,\ \ldots,\ \boldsymbol{k}' \cdot \boldsymbol{k} = n_3. \tag{A2-6}$$

As $\boldsymbol{k}' = (\sin\chi \cos D, \sin\chi \sin D, \cos\chi)$ in the geographic coordinate system,

$$\boldsymbol{k}' \cdot \boldsymbol{k} = n_3 = \cos\chi, \tag{A2-7}$$

$$\boldsymbol{k}' \cdot \boldsymbol{i} = l_3 = \sin\chi \cos D, \tag{A2-8}$$

and

$$\boldsymbol{k}' \cdot \boldsymbol{j} = m_3 = \sin\chi \sin D. \tag{A2-9}$$

As x'-axis is perpendicular to y-axis,

$$\boldsymbol{i}' \cdot \boldsymbol{j} = m_1 = 0. \tag{A2-10}$$

We obtain a transformation matrix from eq. (A2-2) through eq. (A2-10).

$$\left.\begin{aligned}
l_1 &= \cos\chi / \sqrt{1 - \sin^2\chi \sin^2 D}, \\
l_2 &= -\sin^2\chi \cos D \sin D / \sqrt{1 - \sin^2\chi \sin^2 D}, \\
l_3 &= \sin\chi \cos D, \\
m_1 &= 0, \\
m_2 &= \sqrt{1 - \sin^2\chi \sin^2 D}, \\
m_3 &= \sin\chi \sin D, \\
n_1 &= -\sin\chi \cos D / \sqrt{1 - \sin^2\chi \sin^2 D}, \\
n_2 &= -\sin\chi \cos\chi \sin D / \sqrt{1 - \sin^2\chi \sin^2 D}, \\
n_3 &= \cos\chi.
\end{aligned}\right\} \tag{A2-11}$$

The rocket spin axis rotates around the precession axis (z'-axis). The angle, ζ, between the spin axis and the precession axis is given by

$$\zeta = \xi_{\max} - \eta. \tag{A2-12}$$

We consider three components of the spin-axis unit-vector $\boldsymbol{e}_{s'}(e_{sx'}, e_{sy'}, e_{sz'})$ in (x', y', z') coordinates. Let the angular velocity of the rocket precession be Ω (see Fig. A5).

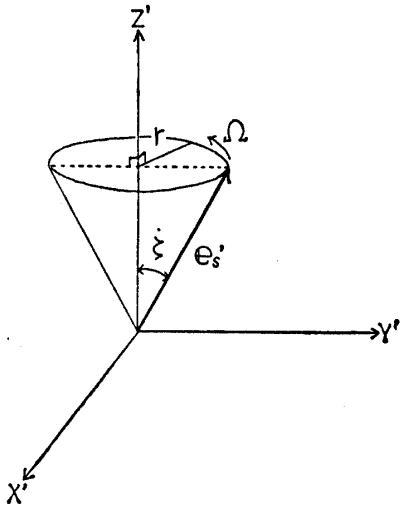

Fig. A5. Coordinate system which explains the rocket precession.

$$\left.\begin{aligned} e_{sx'} &= r\cos(\Omega t+\alpha), \\ e_{sy'} &= r\sin(\Omega t+\alpha), \\ e_{sz'} &= 1-r^2, \end{aligned}\right\} \tag{A2-13}$$

where

$$\frac{r}{\sqrt{1-r^2}}=\tan\zeta, \tag{A2-14}$$

and α is an initial phase of the rocket precession.

We express three components of the rocket spin-axis vector in the geographic coordinate system, $e_s=(e_{sx}, e_{sy}, e_{sz})$;

$$\begin{pmatrix} e_{sx} \\ e_{sy} \\ e_{sz} \end{pmatrix} = \begin{pmatrix} l_1 & l_2 & l_3 \\ m_1 & m_2 & m_3 \\ n_1 & n_2 & n_3 \end{pmatrix} \begin{pmatrix} e_{sx'} \\ e_{sy'} \\ e_{sz'} \end{pmatrix}, \tag{A2-15}$$

that is,

$$\begin{pmatrix} e_{sx} \\ e_{sy} \\ e_{sz} \end{pmatrix} = \begin{pmatrix} \dfrac{\cos\chi}{A} & -\dfrac{\sin^2\chi\cos D\sin D}{A} & \sin\chi\cos D \\ 0 & A & \sin\chi\sin D \\ -\dfrac{\sin\chi\cos D}{A} & -\dfrac{\sin\chi\cos\chi\sin D}{A} & \cos\chi \end{pmatrix} \begin{pmatrix} r\cos(\Omega t+\alpha) \\ r\sin(\Omega t+\alpha) \\ 1-r^2 \end{pmatrix}, \tag{A2-16}$$

where

$$A=\sqrt{1-\sin^2\chi\,\sin^2 D}.$$

We consider a rocket-precession initial phase α. At $t=t_0$, the angle, ξ, between the spin axis and the geomagnetic field line becomes minimum. We use the precession coordinate system. Then, the geomagnetic field vector $\boldsymbol{B}(B_x, B_y, B_z)$ is transformed to $\boldsymbol{B}'(B_{x'}, B_{y'}, B_{z'})$ through eq. (A2-1). From Fig. A6, at $t=t_0$,

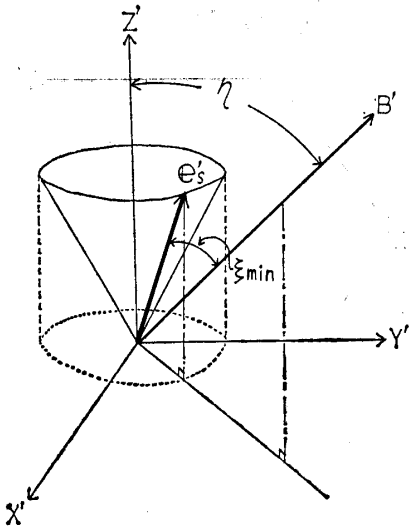

Fig. A6. Diagram for determination of the initial phase of the rocket precession.

$$\frac{e_{sy'}}{e_{sx'}}=\frac{B_{y'}}{B_{x'}}. \tag{A2-17}$$

Therefore,

$$\frac{r\sin(\Omega t_0+\alpha)}{r\cos(\Omega t_0+\alpha)}=\frac{B_{y'}}{B_{x'}}. \tag{A2-18}$$

$$\tan(\Omega t_0+\alpha)=\frac{B_{y'}}{B_{x'}}. \tag{A2-19}$$

From eq. (A2-19)

$$\alpha=\mathrm{Arctan}\left(\frac{B_{y'}}{B_{x'}}\right)-\Omega t_0. \tag{A2-20}$$

A3. The calculation of three components of the electric field $\boldsymbol{E}'_R$ which is observed in the spin plane of the rocket

The rocket spin plane is a plane perpendicular to the spin axis. As the antenna probes rotate in this spin plane, the observed electric field $\boldsymbol{E}'_R$ is included in the spin plane.

A3.1. The projection of an arbitrary vector $\boldsymbol{a}$ on the spin plane

Let $\boldsymbol{a}$ be an arbitrary vector, then the component of $\boldsymbol{a}$ in the direction of the spin axis vector $\boldsymbol{e}_s$ is given by

$$\boldsymbol{a}_s=(\boldsymbol{a}\cdot\boldsymbol{e}_s)\boldsymbol{e}_s. \tag{A3-1}$$

The component of $\boldsymbol{a}$ in the spin plane, $\boldsymbol{a}_R$, is given by

$$\boldsymbol{a}_R=\boldsymbol{a}-\boldsymbol{a}_s=\boldsymbol{a}-(\boldsymbol{a}\cdot\boldsymbol{e}_s)\boldsymbol{e}_s. \tag{A3-2}$$

If $\boldsymbol{a}=(a_x, a_y, a_z)$, the vector $\boldsymbol{a}_R(a_{Rx}, a_{Ry}, a_{Rz})$ projected on the spin plane can be written as

$$\left.\begin{aligned} a_{Rx}&=a_x-(\boldsymbol{a}\cdot\boldsymbol{e}_s)e_{sx},\\ a_{Ry}&=a_y-(\boldsymbol{a}\cdot\boldsymbol{e}_s)e_{sy},\\ a_{Rz}&=a_z-(\boldsymbol{a}\cdot\boldsymbol{e}_s)e_{sz}. \end{aligned}\right\} \tag{A3-3}$$

A3.2. The observed electric field

We measure an amplitude of the electric field, E_R, and an angle θ between the electric field and the geomagnetic field in the spin plane. As the observed electric field $\boldsymbol{E}_R(E_{Rx}, E_{Ry}, E_{Rz})$ is perpendicular to the spin axis,

$$\boldsymbol{E}_R\cdot\boldsymbol{e}_s=0,$$

that is,

$$E_{Rx}\,e_{sx}+E_{Ry}\,e_{sy}+E_{Rz}\,e_{sz}=0. \tag{A3-4}$$

From eq. (A3-3), the geomagnetic field $\boldsymbol{B}_R(B_{Rx}, B_{Ry}, B_{Rz})$ projected on the spin plane is given by

$$\left.\begin{aligned} B_{Rx}&=B_x-(\boldsymbol{B}\cdot\boldsymbol{e}_s)e_{sx},\\ B_{Ry}&=B_y-(\boldsymbol{B}\cdot\boldsymbol{e}_s)e_{sy},\\ B_{Rz}&=B_z-(\boldsymbol{B}\cdot\boldsymbol{e}_s)e_{sz}. \end{aligned}\right\} \tag{A3-5}$$

The relation between $\boldsymbol{E}_R$ and $\boldsymbol{B}_R$ yields

$$\begin{aligned}\boldsymbol{E}_R\cdot\boldsymbol{B}_R&=|\boldsymbol{E}_R|\;|\boldsymbol{B}_R|\cos\theta\\ &=E_{Rx}B_{Rx}+E_{Ry}B_{Ry}+E_{Rz}B_{Rz}\end{aligned} \tag{A3-6}$$

and

$$E_{Rx}^2+E_{Ry}^2+E_{Rz}^2=E_R^2. \tag{A3-7}$$

We calculate E_{Rx}, E_{Ry}, E_{Rz} from eqs. (A3-4), (A3-6) and (A3-7). The solutions are given by

$$E_{Rx}=\frac{-Q\pm\sqrt{Q^2-4PR}}{2P}, \tag{A3-8}$$

$$E_{Ry}=\frac{\Gamma-E_{Rx}\left(B_{Rx}-\dfrac{e_{sx}}{e_{sz}}B_{Rz}\right)}{B_{Ry}-\dfrac{e_{sy}}{e_{sz}}B_{Rz}}, \tag{A3-9}$$

$$E_{Rz}=-\frac{e_{sx}E_{Rx}+e_{sy}E_{Ry}}{e_{sz}}, \tag{A3-10}$$

where

$$P=\left\{\left(1+\frac{{e_{sx}}^2}{{e_{sz}}^2}\right)+\left(1+\frac{{e_{sy}}^2}{{e_{sz}}^2}\right)\frac{(e_{sz}B_{Rx}-e_{sx}B_{Rz})^2}{(e_{sz}B_{Ry}-e_{sy}B_{Rz})^2}\right.$$
$$\left.-\frac{2e_{sx}e_{sy}(e_{sz}B_{Ry}-e_{sx}B_{Rz})}{{e_{sz}}^2(e_{sz}B_{Ry}-e_{sy}B_{Rz})}\right\}, \tag{A3-11}$$

$$Q=\frac{2\Gamma}{(e_{sz}B_{Ry}-e_{sy}B_{Rz})}\left\{\frac{e_{sx}e_{sy}}{e_{sz}}-\left(1+\frac{{e_{sy}}^2}{{e_{sz}}^2}\right)\frac{e_{sz}(e_{sz}B_{Rx}-e_{sx}B_{Rz})}{e_{sz}B_{Ry}-e_{sy}B_{Rz}}\right\}, \tag{A3-12}$$

$$R=\left(1+\frac{{e_{sy}}^2}{{e_{sz}}^2}\right)\frac{{e_{sz}}^2\Gamma^2}{(e_{sz}B_{Ry}-e_{sy}B_{Rz})^2}-{E_R}^2, \tag{A3-13}$$

$$\Gamma=|\boldsymbol{E}_R|\ |\boldsymbol{B}_R|\cos\theta. \tag{A3-14}$$

In order to determine the sign $\pm$ in eq. (A3-8), we calculate the x component of $\boldsymbol{B}_R\times\boldsymbol{E}_R$,

$$(\boldsymbol{B}_R\times\boldsymbol{E}_R)_x=|\boldsymbol{B}_R|\ |\boldsymbol{E}_R|\sin\theta. \tag{A3-15}$$

On the other hand,

$$(\boldsymbol{B}_R\times\boldsymbol{E}_R)_x=B_{Ry}E_{Rz}-B_{Rz}E_{Ry}. \tag{A3-16}$$

We can calculate eq. (A3-16) for two cases of E_{Rx}, respectively. And then we determine $\boldsymbol{E}_R$ is what is consistent with eq. (A3-15).

A4. The subtraction of the induced electric field $\boldsymbol{V}\times\boldsymbol{B}$

The electric field which the rocket of the velocity $\boldsymbol{V}$ observes is given by

$$\boldsymbol{E}=\boldsymbol{E}_q+\boldsymbol{V}\times\boldsymbol{B}. \tag{A4-1}$$

Therefore, the electric field $\boldsymbol{E}_q$ in the geographic coordinate system is given by

$$\boldsymbol{E}_q=\boldsymbol{E}-\boldsymbol{V}\times\boldsymbol{B}. \tag{A4-2}$$

The ambient electric field projected on the spin plane, $\boldsymbol{E}_{qR}$, is given by

$$\boldsymbol{E}_{qR}=\boldsymbol{E}_R-(\boldsymbol{V}\times\boldsymbol{B})_R. \tag{A4-3}$$

$\boldsymbol{E}_R$ is obtained in Appendix Section A3. After we calculate three components of $\boldsymbol{V}\times\boldsymbol{B}$, we obtain three components of $(\boldsymbol{V}\times\boldsymbol{B})_R$ from eq. (A3-3).

$$\boldsymbol{E}_{qR}=\begin{pmatrix} E_{qRx} \\ E_{qRy} \\ E_{qRz} \end{pmatrix}=\begin{pmatrix} E_{Rx}-(\boldsymbol{V}\times\boldsymbol{B})_{Rx} \\ E_{Ry}-(\boldsymbol{V}\times\boldsymbol{B})_{Ry} \\ E_{Rz}-(\boldsymbol{V}\times\boldsymbol{B})_{Rz} \end{pmatrix}. \tag{A4-3}'$$

A5. The assumption of the electric field parallel to the geomagnetic field line

If we are not able to measure the electric field E_s parallel to the spin axis, we must assume the electric field E_B parallel to the geomagnetic field line and obtain the electric field $\boldsymbol{E}_s$ from which we do not need to subtract the induced electric field $\boldsymbol{V}\times\boldsymbol{B}$.

$$\boldsymbol{E}_q=\boldsymbol{E}_{qR}+\boldsymbol{E}_s, \tag{A5-1}$$

where

$$\boldsymbol{E}_s=E_s\boldsymbol{e}_s. \tag{A5-2}$$

According to the assumption,

$$\boldsymbol{E}_q\cdot\boldsymbol{e}_B=E_B. \tag{A5-3}$$

Then,

$$\boldsymbol{E}_{qR}\cdot\boldsymbol{e}_B+\boldsymbol{E}_s\cdot\boldsymbol{e}_B=E_B, \tag{A5-4}$$

that is,

$$E_s(\boldsymbol{e}_s\cdot\boldsymbol{e}_B)=E_B-\boldsymbol{E}_{qR}\cdot\boldsymbol{e}_B. \tag{A5-5}$$

From eq. (A5-5) we obtain the value of E_s;

$$E_s=\frac{E_B-(E_{qRx}e_{Bx}+E_{qRy}e_{By}+E_{qRz}e_{Bz})}{e_{sx}e_{Bx}+e_{sy}e_{By}+e_{sz}e_{Bz}}. \tag{A5-6}$$

Therefore, three components of $\boldsymbol{E}_q$ are given by

$$\boldsymbol{E}_g=\begin{pmatrix} E_{gx} \\ E_{gy} \\ E_{gz} \end{pmatrix}=\begin{pmatrix} E_{gRx}+E_s e_{sx} \\ E_{gRy}+E_s e_{sy} \\ E_{gRz}+E_s e_{sz} \end{pmatrix}. \tag{A5-7}$$

$\boldsymbol{E}_g$ is the electric field vector in the geographic coordinate system. Let the declination be D_e, then the electric field in the magnetic coordinate system $\boldsymbol{E}_m$ is given by

$$\boldsymbol{E}_m=\begin{pmatrix} E_{mx} \\ E_{my} \\ E_{mz} \end{pmatrix}=\begin{pmatrix} \cos D_e & -\sin D_e & 0 \\ \sin D_e & \cos D_e & 0 \\ 0 & 0 & 1 \end{pmatrix}\begin{pmatrix} E_{gx} \\ E_{gy} \\ E_{gz} \end{pmatrix}. \tag{A5-8}$$

In case we measure the electric field E_s parallel to the spin axis, we do not need to assume the electric field E_B. The observed electric field $\boldsymbol{E}_s$ parallel to the spin axis is given by

$$\boldsymbol{E}_s=E_s\boldsymbol{e}_s. \tag{A5-9}$$

Let $\boldsymbol{E}_{gs}$ be the ambient electric field projected on the spin axis,

$$\boldsymbol{E}_{gs}=\boldsymbol{E}_s-(\boldsymbol{V}\times\boldsymbol{B})_s, \tag{A5-10}$$

or

$$\begin{pmatrix} E_{gsx} \\ E_{gsy} \\ E_{gsz} \end{pmatrix}=\begin{pmatrix} E_{sx}-(\boldsymbol{V}\times\boldsymbol{B})_{sx} \\ E_{sy}-(\boldsymbol{V}\times\boldsymbol{B})_{sy} \\ E_{sz}-(\boldsymbol{V}\times\boldsymbol{B})_{sz} \end{pmatrix}, \tag{A5-10}'$$

where $(\boldsymbol{V}\times\boldsymbol{B})_s=(\boldsymbol{V}\times\boldsymbol{B})\cdot\boldsymbol{e}_s$. From eqs. (A4-3) and (A5-10), we obtain the electric field in the geographic coordinate system as follows;

$$\boldsymbol{E}_g=\boldsymbol{E}_{gR}+\boldsymbol{E}_{gs}. \tag{A5-11}$$